Reduced-Order Modelling for Coupled Thermal-Mechanical Analysis and Reliability Assessment of Power Electronic Modules with Nonlinear Material Behaviours

Sheikh Hassan[1,*], Stoyan Stoyanov[1], Pushparajah Rajaguru[1], Christopher Bailey[2]
[1]*School of Computing and Mathematical Sciences, University of Greenwich, London, United Kingdom.*
[2]*School of Electrical, Computer and Energy Engineering, Arizona State University, Arizona, United States.*
[*]*Corresponding Author: s.r.hassan@greenwich.ac.uk.*

***Abstract*—This paper presents a compact and time-efficient reduced-order modelling method for thermal-mechanical analysis and material nonlinearity study of power electronics modules (PEMs). Generally, the thermal-mechanical analyses in research are conducted utilising a sequential coupling method, where the thermal model is solved first, and the temperature distributions are used as a load in the structural (mechanical) system. The direct-coupling method has been employed in the present thermomechanical analysis to evaluate the thermal and structural governing equations together, i.e., to solve for its thermal and directional deformation distributions, which are degrees of freedom (DOFs) of the coupled system. A new approach, utilising the Krylov-subspace- and Arnoldi-based model order reduction (MOR) technique, Newmark method and Newton-Raphson algorithm within the reduced-order modelling framework, has been developed and demonstrated here for analysing material nonlinearity of PEMs. The reduced-order model (ROM) solutions agree exceptionally well with the full-order (FOM) solutions, showing excellent consistency in inelastic strains and plastic work results for materials with time-independent and time-dependent nonlinearities. The MOR method offers a remarkably compact model with a ROM order of just 20x20 for reduced-order computation compared to a FOM order of about 400,000x400,000 and up to 83% reduction in computational time.**

***Index Terms*—Finite Element Method (FEM), Thermal-Mechanical Analysis, Power Electronics Module (PEM), Model Order Reduction (MOR), Reliability Assessment.**

I. Introduction

One of the most critical aspects of technologies in industries, e.g., space and defence, energy, renewable energies, and transportation, is operational reliability, and reliability analysis is required to ensure their safety and operational efficiency. Fortunately, numerical methods can imitate the behaviours of different physical domains for comprehensive analyses and design objectives. The field of engineering sciences, along with its associated partial differential equations (PDEs), can effectively describe the physical behaviours of systems. The finite element method/analysis (FEM/FEA) has been widely utilised as a computational method to solve PDEs. The FEM transforms the PDEs into semi-discrete algebraic systems of unknown variables, and these discretised models are complex and high-dimensional differential equations for most physical modelling scenarios [1]. While FEM offers excellent predictions, it poses challenges in terms of computational time requirements for simulating large-scale models or exploring design points, making model order reduction (MOR) essential. In current MOR applications, the Krylov subspace-based methods have been generally employed due to their "semi-automatic" nature, in contrast to the classic MOR method, i.e., the Modal truncation approaches [2, 3].

The thermal performance of electric systems can lead to decreased performance and reliability issues. In a previous study, Eblen [4] conducted a reliability assessment of electronic components using a thermal-mechanical analysis utilising FEM and CARES, a life prediction computational tool. Codecasa et al. [5] demonstrated thermal-mechanical stresses of an electronic package, decreasing computational time requirements with extended-TRIC, an ad hoc projection-based solver. Shen and Ke [6] expanded the coupled thermo-mechanical investigation to an electrical-thermal-mechanical (ETM) investigation to inspect an electrical contact zone. Feng et al. [7] developed a FEM-based computational technique for the multi-physical modelling of an IGBT module, simulating ETM behaviours and addressing accuracy, convergence, and computing efficiency.

Reduced order modelling of multi-physical systems is vital since coupled systems have relatively higher complexity. The Krylov subspace-based MOR approach was utilised in the work of Choi et al. [8] to develop a reduced-order model (ROM) of a micro-resonator structure for its thermal-mechanical analysis. Similarly, Krylov subspace-based MOR algorithms were implemented in a reduced-order modelling study by Rajaguru et al. [9] to investigate the electrical-thermal aspects of a power electronics module (PEM). Additionally, Binion and Chen [10] analysed the ETM characteristics of a MEMS microgripper, exploring the Krylov subspace-based MOR methods.

In-depth physical aspects analysis involves considering nonlinear behaviours in the model. Hence, reduced-order modelling for nonlinearity assessments can be beneficial to address additional time requirements in nonlinear computation. Scognamillo et al. [11] explored the nonlinear thermal activities of a PEM by carrying out an electrical-thermal study with a MOR code FANTASTIC. Schütz et al. [12] developed a Krylov subspace-based ROM of a piezoelectric actuator for examining its coupled physical conducts while considering nonlinear inputs in the system. Recently, the parametrised temperature-

dependent material properties and the time-independent material nonlinearity of a directly coupled thermal-mechanical PEM model have been investigated with the Krylov subspace-based reduced-order modelling approach [13]–[15].

In the above-referenced literature, the coupled multi-physical, i.e., thermal-mechanical, behaviours have been widely studied by sequentially coupling the models for reduced-order modelling works. However, directly coupling the models would provide a more practical and accurate understanding of the system and should also be practised during reduced-order modelling of coupled systems. Therefore, in this work, the direct coupling method has been considered to evaluate thermal and structural equations simultaneously for the reduced-order modelling in the thermomechanical analysis of the PEM. The temperature-dependency of material properties has been taken into consideration for this work, too, as prior reduced-order modelling studies mainly used constant material properties. The time-independent material nonlinearity, i.e., plasticity, and time-dependent material nonlinearity, i.e., creep and viscoplasticity, of PEM's wires and solders have been studied here with the reduced-order modelling method. A new reduced-order modelling method has been presented in this work to study these material nonlinearities. The Newmark time-integration technique for transient analysis, the Newton-Rhapson method for nonlinear iteration and the second-order Arnoldi (SOAR) algorithm for MOR have been coupled within the formulated Krylov subspace-based reduced-order modelling technique.

II. Problem Formulation

A. Full-Order Model (FOM)

The discretised coupled thermal-mechanical system, for nonlinear analysis, can be expressed as [16, 17]:

$$\begin{aligned} &\boldsymbol{M}\ddot{\boldsymbol{z}}(t) + \boldsymbol{D}\dot{\boldsymbol{z}}(t) + \boldsymbol{f}(\boldsymbol{z}(t)) = \boldsymbol{G}\boldsymbol{u}(t) \\ &\boldsymbol{y}(t) = \boldsymbol{L}\boldsymbol{z}(t) \end{aligned} \tag{1}$$

Here, $\boldsymbol{M}, \boldsymbol{D} \in \mathbb{R}^{n\times n}$ represent mass and damping matrices, while $\boldsymbol{f}(\boldsymbol{z}(t)), \boldsymbol{G} \in \mathbb{R}^{n\times M}$, and $\boldsymbol{L} \in \mathbb{R}^{P\times n}$, are internal load, input (external load), and output matrices. Furthermore, $\boldsymbol{u}(t) \in \mathbb{R}^M$, $\boldsymbol{y}(t) \in \mathbb{R}^P$, and $\boldsymbol{z}(t) \in \mathbb{R}^n$ depict inputs, outputs and states of the system, and they are time (t) dependent. For the nonlinear model, $\boldsymbol{f}(\boldsymbol{z}(t))$ and initial tangent stiffness matrix, $\boldsymbol{K}(\boldsymbol{z}(t)) \in \mathbb{R}^{n\times n}$, depend on the states ($\boldsymbol{z}(t)$) of the system. In a general thermal-mechanical model, matrix components can be characterised as [17, 18]:

$$\begin{aligned} &\boldsymbol{M} = \begin{bmatrix} \boldsymbol{M}_s & \boldsymbol{0} \\ \boldsymbol{0} & \boldsymbol{0} \end{bmatrix}, \boldsymbol{D} = \begin{bmatrix} \boldsymbol{D}_s & \boldsymbol{0} \\ \boldsymbol{D}^{tu} & \boldsymbol{D}^{t} \end{bmatrix}, \boldsymbol{K} = \begin{bmatrix} \boldsymbol{K}_s & \boldsymbol{K}^{ut} \\ \boldsymbol{0} & \boldsymbol{K}^{t} \end{bmatrix}, \\ &\boldsymbol{G} = \begin{bmatrix} \boldsymbol{F}^{a} \\ \boldsymbol{Q} \end{bmatrix}, \ddot{\boldsymbol{z}} = \begin{bmatrix} \ddot{\boldsymbol{z}}_{ut} \\ \ddot{\boldsymbol{T}} \end{bmatrix}, \dot{\boldsymbol{z}} = \begin{bmatrix} \dot{\boldsymbol{z}}_{ut} \\ \dot{\boldsymbol{T}} \end{bmatrix}, \boldsymbol{z} = \begin{bmatrix} \boldsymbol{z}_{ut} \\ \boldsymbol{T} \end{bmatrix} \end{aligned} \tag{2}$$

$$\text{with,} \quad \begin{aligned} &\boldsymbol{K}^t = \boldsymbol{K}^{tb} + \boldsymbol{K}^{tc}, \boldsymbol{F}^a = \boldsymbol{F}^{nd} + \boldsymbol{F}^{pr} + \boldsymbol{F}^{ac}, \\ &\boldsymbol{Q} = \boldsymbol{Q}^{nd} + \boldsymbol{Q}^{g} + \boldsymbol{Q}^{c} \end{aligned} \tag{3}$$

In this context, $\boldsymbol{M}_s$ refers to the structural mass matrix, whilst $\boldsymbol{D}_s$, $\boldsymbol{D}^{tu}$, and $\boldsymbol{D}^t$ represent the corresponding matrices for structural and thermoelastic damping and thermal-specific heat. Similarly, $\boldsymbol{K}_s$, $\boldsymbol{K}^{ut}$, and $\boldsymbol{K}^t$ denote the stiffness matrices for structural and thermoelastic properties and thermal conductivity, respectively. Additionally, $\boldsymbol{K}^{tb}$ and $\boldsymbol{K}^{tc}$ signify the thermal conductivity matrices of material and convection surface. The mechanical (structural) load vectors are denoted by $\boldsymbol{F}^a$, whilst nodal force and pressure load vectors and force vectors because of acceleration are represented by $\boldsymbol{F}^{nd}$, $\boldsymbol{F}^{pr}$, and $\boldsymbol{F}^{ac}$, respectively. The thermal load vector is characterised by $\boldsymbol{Q}$, and nodal heat flow rate and convection surface vectors and heat generation rate vector, excluding Joule heating, are specified by $\boldsymbol{Q}^{nd}$, $\boldsymbol{Q}^{c}$, and $\boldsymbol{Q}^{g}$, respectively. Finally, $\boldsymbol{z}_{ut}$ and $\boldsymbol{T}$ designate the potential displacement and thermal vectors.

B. Reduced-Order Model (ROM)

By implementing the model order reduction (MOR) algorithm, it is possible to obtain a reduced-order model (ROM) for the system described in (1). This ROM can be expressed in a more concise form, resulting in a more efficient system, as in the following [19]–[21]:

$$\begin{aligned} &\boldsymbol{M}_r\ddot{\boldsymbol{z}}_r(t) + \boldsymbol{D}_r\dot{\boldsymbol{z}}_r(t) + \boldsymbol{f}_r(\boldsymbol{z}_r(t)) = \boldsymbol{G}_r\boldsymbol{u}_r(t) \\ &\boldsymbol{y}_r(t) = \boldsymbol{L}_r\boldsymbol{z}_r(t) \end{aligned} \tag{4}$$

The Krylov subspace-based MOR method, with the second-order Arnoldi (SOAR) algorithm, has been used to obtain the reduced-order matrices in (4). The transformation to reduced space involves performing the following operations: $\boldsymbol{M}_r = \boldsymbol{V}^T\boldsymbol{M}\boldsymbol{V}$, $\boldsymbol{D}_r = \boldsymbol{V}^T\boldsymbol{D}\boldsymbol{V}$, $\boldsymbol{K}_r = \boldsymbol{V}^T\boldsymbol{K}\boldsymbol{V}$ and hence subsequently $\boldsymbol{f}_r = \boldsymbol{V}^T\boldsymbol{f}$, $\boldsymbol{G}_r = \boldsymbol{V}^T\boldsymbol{G}$ and $\boldsymbol{L}_r = \boldsymbol{L}\boldsymbol{V}$ [19]–[21]. The inputs, outputs, and states of the reduced-order model are denoted by $\boldsymbol{u}_r(t) \in \mathbb{R}^m$, $\boldsymbol{y}_r(t) \in \mathbb{R}^p$, and $\boldsymbol{z}_r(t) \in \mathbb{R}^q$, respectively. The reduced-order system matrices, $\boldsymbol{M}_r, \boldsymbol{D}_r, \boldsymbol{K}_r \in \mathbb{R}^{q\times q}$, internal load and input (external load) matrix, $\boldsymbol{f}_r, \boldsymbol{G}_r \in \mathbb{R}^{q\times m}$, and output matrix, $\boldsymbol{L}_r \in \mathbb{R}^{p\times q}$, have a much lower order than the full-order matrices, i.e., $q \ll n$. This reduction in order has been achieved using the transformation matrix $\boldsymbol{V} \in \mathbb{R}^{n\times q}$, which has been obtained from the transfer function of the FOM in (1) as [19, 20]:

$$\boldsymbol{Y}(s) = \boldsymbol{L}(s^2\boldsymbol{M} + s\boldsymbol{D} + \boldsymbol{K})^{-1}\boldsymbol{G} \tag{5}$$

$$\boldsymbol{Y}_r(s) = \boldsymbol{L}_r(s^2\boldsymbol{M}_r + s\boldsymbol{D}_r + \boldsymbol{K}_r)^{-1}\boldsymbol{G}_r \tag{6}$$

Here, the transfer function of the ROM can be subsequently determined using the ROM in (4). The ROM in (4) has been solved by Newmark and Newton-Rhapson methods [17, 22].

C. ROM: Newmark & Newton-Raphson Methods

The reduced system's applied load, stated in (4), is denoted by $\boldsymbol{G}_r\boldsymbol{u}_r(t)$ and can be represented by a discrete set of values of $\boldsymbol{G}_r\boldsymbol{u}_r(t_i)$, where i ranges from 0 to i_{max}. This set of values represents time intervals as [17, 22]:

$$\Delta t_i = t_{i+1} - t_i \tag{7}$$

The responses of (4) are resolved for discrete time intervals, referred to as time instants t_i at time i. The system's states, $\boldsymbol{z}_r(t_i)$, $\dot{\boldsymbol{z}}_r(t_i)$, and $\ddot{\boldsymbol{z}}_r(t_i)$, are assumed to be known for initial time instant and satisfy (4) at time t_i. The internal

force (load) of the reduced system at time t_i, denoted by $\boldsymbol{f}_r(t_i)$, is initialised by $\boldsymbol{K}_r\boldsymbol{z}_r(t_i)$ and subsequently updated based on the preceding states $\boldsymbol{z}_r$, $\dot{\boldsymbol{z}}_r$ and $\ddot{\boldsymbol{z}}_r$ at time i. In the current numerical computations, the responses for state quantities $\boldsymbol{z}_r(t_{i+1})$, $\dot{\boldsymbol{z}}_r(t_{i+1})$ and $\ddot{\boldsymbol{z}}_r(t_{i+1})$ will be resolved for the time t_{i+1} that satisfy (4) at that time, t_{i+1}, as [17, 22]:

$$\begin{aligned}\boldsymbol{M}_r\ddot{\boldsymbol{z}}_r(t_{i+1}) + \boldsymbol{D}_r\dot{\boldsymbol{z}}_r(t_{i+1}) + \boldsymbol{f}_r(\boldsymbol{z}_r(t_{i+1})) \\ = \boldsymbol{G}_r\boldsymbol{u}_r(t_{i+1}) \\ \boldsymbol{y}_r(t_{i+1}) = \boldsymbol{L}_r\boldsymbol{z}_r(t_{i+1})\end{aligned} \tag{8}$$

In the time-stepping process, for $i = \{0, 1, 2, 3, ...\}$, the expected responses at time instances $i = \{1, 2, 3, ...\}$ are obtained in the solution. The known initial states, $\boldsymbol{z}(t_0)$, $\dot{\boldsymbol{z}}(t_0)$, and $\ddot{\boldsymbol{z}}(t_0)$, are a requirment to commence the process.

For describing the nonlinear dynamic analysis procedure, (8) can be composed as [17, 22]:

$$\hat{\boldsymbol{f}}_r(\boldsymbol{z}(t_{i+1})) = \hat{\boldsymbol{u}}_r(t_{i+1}) \tag{9}$$

Here,

$$\begin{aligned}\hat{\boldsymbol{f}}_r(\boldsymbol{z}_r(t_{i+1})) = \boldsymbol{M}_r\ddot{\boldsymbol{z}}_r(t_{i+1}) + \boldsymbol{D}_r\dot{\boldsymbol{z}}_r(t_{i+1}) \\ + \boldsymbol{f}_r(\boldsymbol{z}_r(t_{i+1}))\end{aligned} \tag{10}$$

$$\hat{\boldsymbol{u}}_r(t_{i+1}) = \boldsymbol{G}_r\boldsymbol{u}_r(t_{i+1}) \tag{11}$$

Considering that, after the completion of j cycles in the iteration, an estimation of the state $\boldsymbol{z}_r^{(j)}(t_{i+1})$ has been achieved. The next step of the iterative process will give a better estimation, $\boldsymbol{z}_r^{(j+1)}(t_{i+1})$, with $j = \{1, 2, 3, ...\}$. To accomplish this, the total "internal load" $\hat{\boldsymbol{f}}_r^{(j+1)}(t_{i+1})$ has been expanded in a Taylor series around the available estimation of $\boldsymbol{z}_r^{(j)}(t_{i+1})$, and $\hat{\boldsymbol{f}}_r(t_{i+1})$ has been explained in terms of $\boldsymbol{z}_r(t_{i+1})$, in (9), as [17, 22]:

$$\begin{aligned}\hat{\boldsymbol{f}}_r^{(j+1)}(\boldsymbol{z}_r(t_{i+1})) \simeq \hat{\boldsymbol{f}}_r^{(j)}(t_{i+1}) \\ + \frac{\partial\hat{\boldsymbol{f}}_r}{\partial\boldsymbol{z}_r}\bigg|_{\boldsymbol{z}_r^{(j)}(t_{i+1})} \Delta\boldsymbol{z}_r^{(j)}(t_{i+1}) \\ + \frac{1}{2}\frac{\partial^2\hat{\boldsymbol{f}}_r}{\partial\boldsymbol{z}_r^2}\bigg|_{\boldsymbol{z}_r^{(j)}(t_{i+1})} \Delta\boldsymbol{z}_r^{(j)}(t_{i+1}) + \dots \\ = \hat{\boldsymbol{u}}_r(t_{i+1})\end{aligned} \tag{12}$$

Here,

$$\Delta\boldsymbol{z}_r^{(j)}(t_{i+1}) = \boldsymbol{z}_r^{(j+1)}(t_{i+1}) - \boldsymbol{z}_r^{(j)}(t_{i+1}) \tag{13}$$

Upon differentiation of (10) at the determined state, $\boldsymbol{z}_r^{(j)}(t_{i+1})$, and subsequent deduction of the derivatives by Newmark's approach, the following is obtained [17, 22]:

$$\hat{\boldsymbol{K}}_r^{(j)}(t_{i+1}) \equiv \boldsymbol{A}_r^{(1)} + \boldsymbol{K}_r^{(j)}(\boldsymbol{z}_r(t_{i+1})) \tag{14}$$

Here,

$$\boldsymbol{K}_r^{(j)}(t_{i+1}) = \frac{\partial\boldsymbol{f}_r}{\partial\boldsymbol{z}_r}\bigg|_{\boldsymbol{z}_r(t_{i+1})} \tag{15}$$

$$\hat{\boldsymbol{K}}_r^{(j)}(t_{i+1}) = \frac{\partial\hat{\boldsymbol{f}}_r}{\partial\boldsymbol{z}_r}\bigg|_{\boldsymbol{z}_r(t_{i+1})} \tag{16}$$

Eq. (15) and (16) act in accordance with the definition of the tangent stiffness matrix at $\boldsymbol{z}_r^{(j)}(t_{i+1})$. The Newmark time integration parameter matrix, denoted as $\boldsymbol{A}_r^{(1)}$, in (14) can be defined as [17, 22]:

$$\boldsymbol{A}_r^{(1)} = a_0\boldsymbol{M}_r + a_1\boldsymbol{D}_r \tag{17}$$

Here, a_0 and a_1 are Newmark time integration coefficients.

When considering the state $\boldsymbol{z}_r^{(j)}(t_{i+1})$, if it is in close proximity to the solution, the change in $\boldsymbol{z}_r(t_{i+1})$, i.e., $\Delta\boldsymbol{z}_r^{(j)}(t_{i+1})$ as presented in (13), will be of a small magnitude. In this case, it will be reasonable to disregard the second and higher-order terms of (12), which advances to the linearised equation as in the following [17, 22]:

$$\begin{aligned}\hat{\boldsymbol{f}}_r^{(j+1)}(t_{i+1}) \simeq \hat{\boldsymbol{f}}_r^{(j)}(t_{i+1}) + \hat{\boldsymbol{K}}_r^{(j)}(t_{i+1})\Delta\boldsymbol{z}_r^{(j)}(t_{i+1}) \\ = \hat{\boldsymbol{u}}_r(t_{i+1})\end{aligned} \tag{18}$$

or

$$\begin{aligned}\hat{\boldsymbol{K}}_r^{(j)}(t_{i+1})\Delta\boldsymbol{z}_r^{(j)} = \hat{\boldsymbol{u}}_r(t_{i+1}) - \hat{\boldsymbol{f}}_r^{(j)}(t_{i+1}) \\ \equiv \hat{\boldsymbol{R}}_r^{(j)}(t_{i+1})\end{aligned} \tag{19}$$

Employing the Newmark method to the equation (10) and concurrently incorporating it with the right-hand side of the equation (19) results in the term for residual force as [17, 22]:

$$\begin{aligned}\hat{\boldsymbol{R}}_r^{(j)}(t_{i+1}) = \hat{\boldsymbol{U}}_r(t_{i+1}) - \hat{\boldsymbol{f}}_r^{(j)}(t_{i+1}) \\ - \boldsymbol{A}_r^{(1)}\boldsymbol{z}_r^{(j)}(t_{i+1})\end{aligned} \tag{20}$$

Here,

$$\hat{\boldsymbol{U}}_r(t_{i+1}) = \hat{\boldsymbol{u}}_r(t_{i+1}) + \boldsymbol{M}_r\boldsymbol{A}_r^{(2)}(t_i) + \boldsymbol{D}_r\boldsymbol{A}_r^{(3)}(t_i) \tag{21}$$

with Newmark time integration parameter matrices, $\boldsymbol{A}_r^{(2)}$ and $\boldsymbol{A}_r^{(3)}$, are defined as [17, 22]:

$$\boldsymbol{A}_r^{(2)}(t_i) = a_0\boldsymbol{z}_r(t_i) + a_2\dot{\boldsymbol{z}}_r(t_i) + a_3\ddot{\boldsymbol{z}}_r(t_i) \tag{22}$$

$$\boldsymbol{A}_r^{(3)}(t_i) = a_1\boldsymbol{z}_r(t_i) + a_4\dot{\boldsymbol{z}}_r(t_i) + a_5\ddot{\boldsymbol{z}}_r(t_i) \tag{23}$$

Here, a_0 to a_5 are Newmark time integration coefficients.

III. Power Electronics Module (PEM)

The application of the presented reduced-order modelling approach centred on a *3D* finite-element model of a power electronics module (PEM) structure, examining its thermal-mechanical characteristics for time-independent and time-dependent material nonlinearities. The PEM structure and applied boundary conditions for the direct-coupled thermal-mechanical analysis are presented in Fig. 1. To construct the model in ANSYS, Silicon (*Si*) for semiconductor materials, Aluminium (*Al*) for the wire materials, and *96.5Sn3.5Ag* for solder materials have been selected, here wire and solder materials have nonlinear behaviours.

A. FEM Model

For this investigation, directly coupled thermal-mechanical analysis approach has been considered for the transient FEM modelling. Within the physical model, the *Si* body serves as the thermal source and features an *internal heat generation* boundary condition with generation rate reaching up to $Q_{Si_N} = 1$ normalised unit. The baseplate's bottom surface has a *convection* boundary condition with a convection coefficient

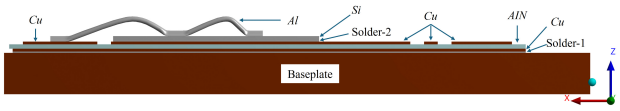

(a) PEM *2D* Front View.

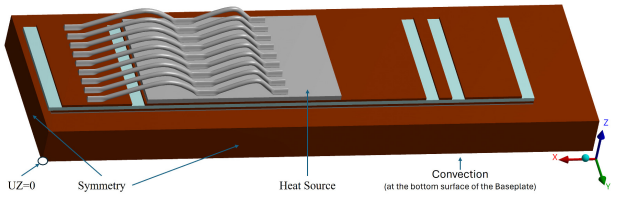

(b) 3D View and The Boundary Conditions.

Fig. 1: PEM Structure and Boundary Conditions.

of about $h_{C_N} = 1$ normalised unit at peak, and the highest ambient temperature of $T_{C_N} = 0.19$ normalised unit, indicating supposed ambient temperatures. The homologous temperature, regarding *Al* materials, in the PEM structure reaches up to ≈ 0.39. The two surfaces of the baseplate along the $+X$ and $+Y$ directions have *symmetry* boundary conditions, while the intersecting bottom node features *fixed displacement* boundary conditions for the Z-axis as $UZ = 0$, with no anticipated deformation, as shown in Fig. 1b. The simulated analysis includes three loading cycles, as shown in Fig. 2. Here, the heat-generating body and the convection surface feature varying generation, coefficient, and temperature values. Parameter data are presented in a normalised (non-dimensional) format to provide a general outlook of the analysis rather than a problem-specific outlook. Temperatures, heat generation rates, and convection coefficients are normalised by dividing their respective values by the maximum observed temperature in the heat source (T_{Si_M}) and the highest generation rate (Q_{Si_M}) and convection coefficient (h_{C_M}) for the *internal heat generation* and *convection* boundary conditions, i.e., $T_{C_N} = T_C/T_{Si_M}$, $Q_{Si_N} = Q_{Si}/Q_{Si_M}$ and $h_{C_N} = h_C/h_{C_M}$, respectively. Material properties data are assigned through ANSYS Workbench, accessed from the ANSYS and Granta Design booklet [23].

The *Al* wire materials and the *96.5Sn3.5Ag* solder materials include nonlinear material behaviours in the FEM model. In particular, the wire materials follow the *bilinear isotropic hardening* rule for plasticity behaviours and *Norton*'s implicit equation for creep behaviours. The bilinear plasticity modelling parameter values are considered based on the approaches described in [17, 24], and the creep modelling parameters are extracted from [25]. Furthermore, the solder materials follow the *Anand* viscoplasticity model for inelastic behaviours, and the modelling parameters are extracted from [26].

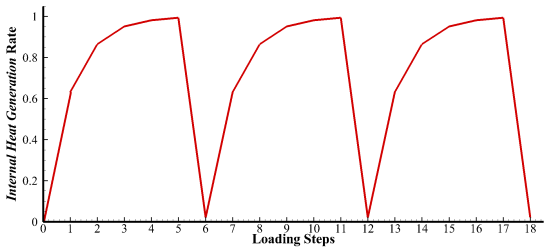

Fig. 2: Normalised *Internal Heat Generation* Rate (Q_{Si_N}) of the Heat-Generating Body During Loading Steps.

B. Reduced Model

The state-space FOM, presented in (1), has a $n = 396,866$ degrees of freedom (DOFs) with system matrices of size $n \times n$. In contrast, the ROM, presented in (4), has a total of $q = 20$ DOFs, with system matrices of size $q \times q$. This significant reduction in DOFs for the ROM facilitates comparatively much faster computation. By incorporating order reductions of system matrices, the reduction process and ROM solution required only $t_{\text{ROM}_N} = 0.17$ normalised time unit, compared to FOM's $t_{\text{FOM}_N} = 1$ normalised time unit, executing both modelling approaches on the same computer. The required times for model solutions are normalised as follows: $t_{\text{ROM}_N} = t_{\text{ROM}}/t_{\text{FOM}}$; $t_{\text{FOM}_N} = t_{\text{FOM}}/t_{\text{FOM}}$; in this operation, t_{ROM} denotes the time needed for reduced-order modelling, including the order reduction process of system matrices, and t_{FOM} represents the time for full-order modelling. Hence, the implementation of the Krylov subspace-based MOR approach has resulted in an impressive 83% decrease in computational time requirements for the exhibited FEM model.

The processes of the reduced-order modelling are summarised in the flow chart depicted in Fig. 3, explaining the organisational technique. The ANSYS computational tool has been utilised for developing the PEM model, FEM discretisation, and attaining the system matrices of the FOM. The system matrices have been imported into MATLAB to create the ROM with the considered Krylov subspace- and Arnoldi-based MOR method.

C. Results and Discussions

The ROM results must correspond with the FOM results to ensure the effectiveness of the reduced-order modelling method. The FEM model's DOFs include temperature and

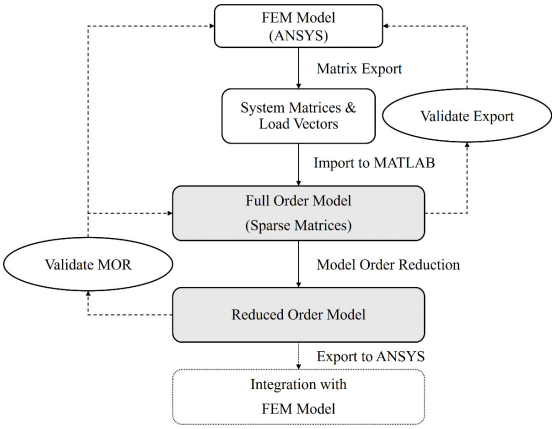

Fig. 3: The Organizational Process of Presented Reduced-Order Modelling Method.

directional deformations, specifically, deformation in the X, Y, and Z-axis. Fig. 4 provides contours of the normalised temperature (T_N) and total deformation (U_N) distributions, evaluating the outcomes of both FOM and ROM. The ROM results exhibit remarkable accuracies when compared to the FOM results.

In Fig. 4a and 4b, it is evident that the wire bond zones on Si encounter some of the highest temperatures. These temperatures can reach the maximum temperature values of the *Si*-based semiconductor. Notably, the *Max* and *Min* temperature values for the PEM structure show only a marginal discrepancy of about 0.1% between the FOM and ROM solutions. Furthermore, in Fig. 4c and 4d, the results obtained from FOM and ROM demonstrate that the difference between their respective solutions amounts to approximately 0.14%, for the maximum total deformation value. The resultant temperatures (T) and total deformations (U) have been normalised through the following operations: $T_N = T/T_{Si_M}$ and $U_N = U/U_M$, respectively. Here, U_M and T_{Si_M} signify the maximum observed values over time in total deformations and temperatures.

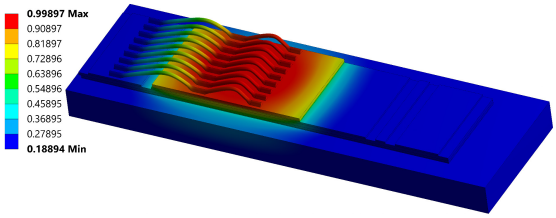

(a) Normalised Temperature, FOM Solution.

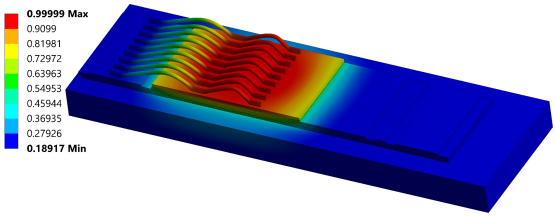

(b) Normalised Temperature, ROM Solution.

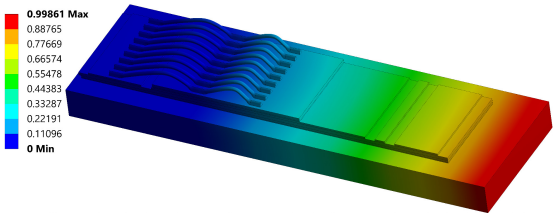

(c) Normalised Total Deformation, FOM Solution.

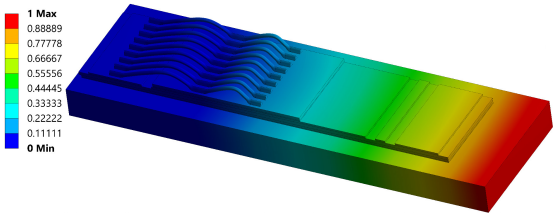

(d) Normalised Total Deformation, ROM Solution.

Fig. 4: Maximum Normalised Temperature (T_N) and Total Deformation (U_N) Distribution Over Time of the PEM Structure.

Fig. 5 shows the normalised equivalent von-Mises stresses (σ_{v_N}) in the evaluated wire bond site (in the wire body). Here, the von-Mises stresses have been normalised as: $\sigma_{v_N} = \sigma_v/\sigma_Y^{(\mathrm{Al})}$, where σ_v is the resulting von-Mises stress and $\sigma_Y^{(\mathrm{Al})}$ is the yield strength of *Al*. These results have been attained from a probing point, a line (*path*) across the wire bond area displayed in Fig. 5a since these are crucial failure sites [27]. The stress results obtained from both the FOM and ROM solutions are compared in Fig. 5b. The stress results obtained from both the FOM and ROM solutions are compared in Fig. 5b. Remarkably, the stress results show a mean disparity of mere 1.85% amid the results received from the ROM and the FOM solutions. Therefore, the demonstrated reduced-order modelling method affirms its suitability for reliability analysis. It is worth noting that the maximum stresses across the probing point go above the 1 normalised unit, which is the yield stress limit of the wire materials.

In Fig. 6, the normalised equivalent plastic strain (ε_N^p) results for the wire bodies, by ROM and FOM solutions, are presented. The plastic strains are normalised as $\varepsilon_N^p = \varepsilon^p/\varepsilon_{eq}$, where ε^p denotes the resultant equivalent plastic strains and ε_{eq} is the resulting equivalent total strains. The results demon-

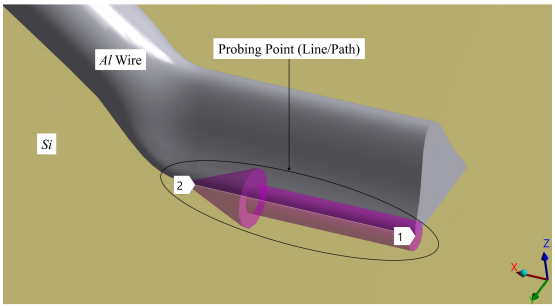

(a) A Probing Point (line/path) in a Wire Bond Site.

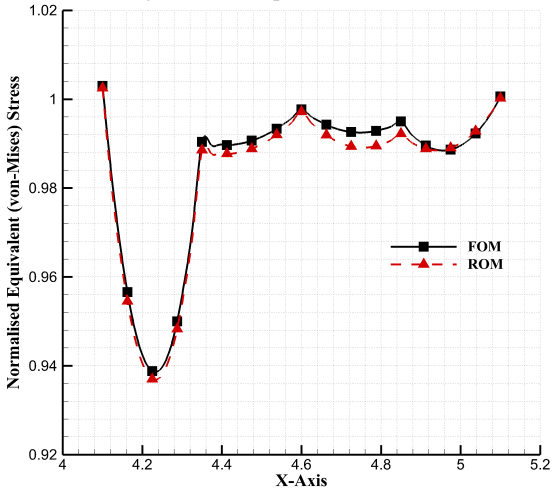

(b) Normalised Equivalent (von-Mises) Stresses.

Fig. 5: Maximum Normalised Equivalent (von-Mises) Stress (σ_{v_N}) Over Time Along a Probing Point in a Wire Bond Site (within the *Al* Wire Body) of the PEM Structure.

strate minimal discrepancies and indicate that the ROM solution can effectively approximate the FOM solution. The plastic strains describe the degree of work hardening, which is the time-independent inelastic deformation characteristics of the materials [24]. As seen in Fig. 6, most plastic strains appear in the wire bond sites on *Si*; this includes the maximum plastic strains. Therefore, wire bond sites on *Si* will potentially face deterioration.

The normalised equivalent creep strain (ε_N^{cr}) results are shown in Fig. 7. The creep strains are normalised as $\varepsilon_N^{cr} = \varepsilon^{cr}/\varepsilon_{eq}$, with ε^{cr} denoting the observed equivalent creep strains. The creep is a type of deformation that occurs under persistent stress over time, most commonly at high temperatures [28]. The outcome obtained via the ROM solution corresponds well with the outcome obtained via the FOM solution, showing slight differences between the distributions. It is seen in Fig. 7 that a large part of the wire materials on *Si* show a comparatively significant amount of creep stains, and the wire bond sites on *Si* show maximum values. The creep strain distributions are consistent with the temperature distributions, as shown in Fig. 4a and 4b, where wires on *Si* showed maximum temperatures. Considering the plastics strains, shown in Fig. 6, and creeep strains, shown in Fig. 7, it is evident that wire bond sites on *Si* are possible failure sites.

Inelastic behaviours of *Solder-2* materials are presented with normalised equivalent inelastic strain (ε_N^{in}) results in Fig. 8, with the results presenting combined time-independent and time-dependent material nonlinearities. The equivalent inelastic strain results are normalised via $\varepsilon_N^{in} = \varepsilon^{in}/\varepsilon_{eq}$, where ε^{in} represents the resulting equivalent inelastic strains. The results obtained by ROM and FOM show good agreement with nominal visual differences in the distribution values. From the results, it is noticeable that *Solder-2* faces a distinct amount of inelastic strains throughout the body, and since this solder

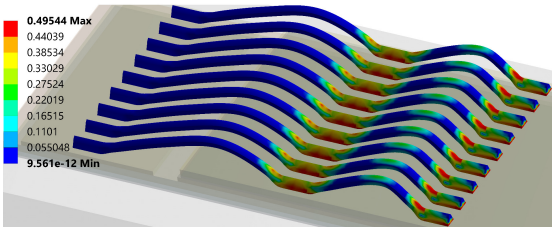

(a) Normalised Equivalent Creep Strain, by FOM.

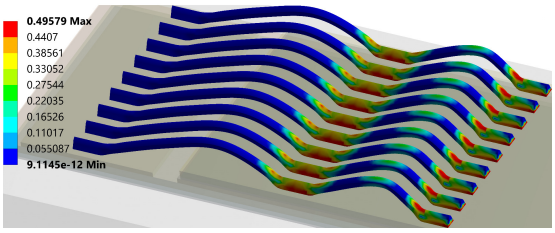

(b) Normalised Equivalent Creep Strain, by ROM.

Fig. 7: Maximum Normalised Equivalent Creep Strain (ε_N^{cr}) Over Time in Wire Bodies of the PEM Structure.

is attached to the heat source *Si*, it is expected. Notably, peak strains are seen in the region where temperature values were high and just below the wire bond sites, as shown in Fig. 4a and 4b, so the heat transfer behaviours of the PEM structure play a vital role in inelastic strains behaviours of the *Solder-2*.

Some more insights into inelastic behaviours are presented with nonlinear inelastic works, displayed in Fig. 9, which describes the work done during the inelastic deformations. The nonlinear inelastic works (W_N^{in}) are normalised by $W_N^{in} = W^{in}/W_M^{in}$, where W^{in} is the resultant inelastic works and W_M^{in} is the maximum detected value in the nonlinear inelastic works. As seen from the results obtained by the ROM and FOM solutions, the ROM solutions can produce an excellent

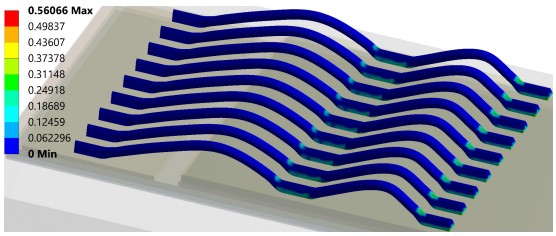

(a) Normalised Equivalent Plastic Strain, by FOM.

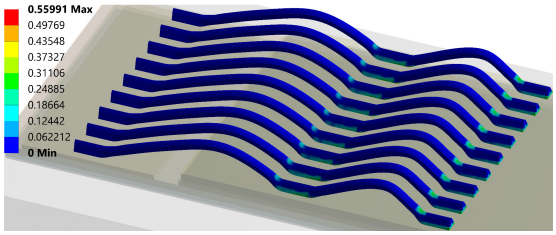

(b) Normalised Equivalent Plastic Strain, by ROM.

Fig. 6: Maximum Normalised Equivalent Plastic Strain (ε_N^{p}) Over Time in Wire Bodies of the PEM Structure.

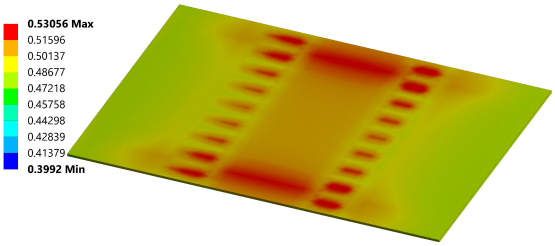

(a) Normalised Equivalent Inelastic Strain, by FOM.

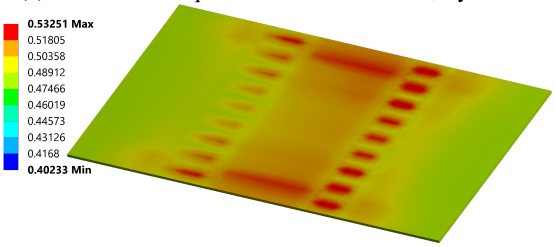

(b) Normalised Equivalent Inelastic Strain, by ROM.

Fig. 8: Maximum Normalised Equivalent Inelastic Strain (ε_N^{in}) Over Time in the *Solder-2* Body of the PEM Structure.

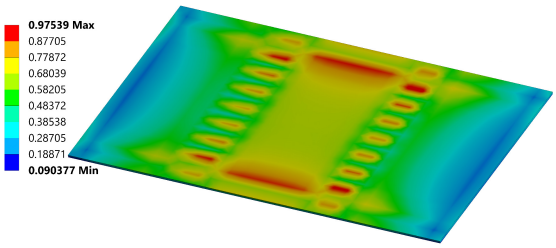

(a) Normalised Nonlinear Inelastic Work, by FOM.

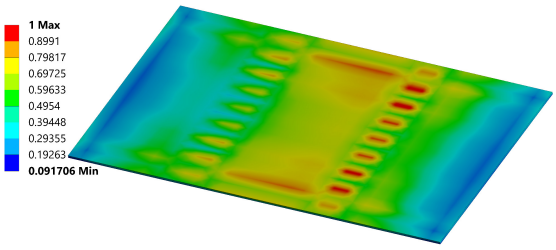

(b) Normalised Nonlinear Inelastic Work, by ROM.

Fig. 9: Normalised Nonlinear Inelastic Work (W_N^{in}) in the *Solder-2* Body of the PEM Structure.

approximation for the inelastic works, with some differences in the distribution values. The distributions of the inelastic works show most of the inelastic works have taken place in the area below the wire bond sites where temperatures are high, which is consistent with the distribution of the inelastic strains, presented in Fig. 8. The results further confirm the importance of heat transfer behaviours in the PEM structure.

D. Reliability Assessment - Life Estimation

1) Strain Based: The Coffin-Manson model, defining the low-cycle fatigues considering inelastic strains, can be inscribed as [29]–[31]:

$$N_f = \frac{1}{2}\left(\frac{1}{\varepsilon'_f}\frac{\Delta\varepsilon^{in}}{2}\right)\frac{1}{c} \tag{24}$$

Here the parameters are: $\Delta\varepsilon^{in}/2$, which represents the accumulated equivalent inelastic strain amplitude (in %) with $\Delta\varepsilon^{in}/2 = \Delta\varepsilon^{p}/2 + \Delta\varepsilon^{cr}/2$, where, $\Delta\varepsilon^{p}/2$ and $\Delta\varepsilon^{cr}/2$ are the accumulated equivalent plastic and creep strain amplitudes, respectively; ε'_f, denoting the fatigue ductility coefficient; $2N_f$, describing the number of reversals to satisfy the failure criterion (with N_f cycles); and c, defining the fatigue ductility exponent. The constants ε'_f and c are determined empirically.

It is essential to establish the failure criteria for estimating the fatigue life of materials. In the case of the chip-solder (*Solder-2*), the failure criteria are the delamination of 20% of the solder area and considered for volume-weighted averaging. For wires, failure criteria are 10% of its area degradation, and this area has been considered for the volume-weighted averaging process [32, 33]. Table I presents the estimated fatigue life values of wires and solder-2 in the PEM structure for ROM and FOM solutions. $\varepsilon'_f = 21.9$ and $c = -0.93$ have been used for life estimation of *96.5Sn3.5Ag* solder, and the values are retrieved from [34]. The values of ε'_f range from 0.16 to 0.20, and the values of c vary from -0.5 to -0.7 for metals, with higher values indicating higher ductility. $\varepsilon'_f = 0.2$ and $c = -0.5$ have been selected to estimate life of *Al* wires since *Al* have excellent ductile characteristics [35]–[37].

TABLE I: Estimated Fatigue Life of Wires and *Solder-2*.

PEM Components	**Estimated Life in Cycles**	
	by FOM Solutions	**by ROM Solutions**
Wires (*Al*)	890	810
Solder-2 (*96.5Sn3.5Ag*)	2,740	2,760

IV. Error Analysis & Optimal Order

The ROM presented in (4) exhibits deviations from its FOM illustrated in (1). The discrepancies in the ROM solutions can be quantified by analysing the transfer functions, detailed in (5) and (6), as in the following [38, 39]:

$$\boldsymbol{\epsilon}(s) = \frac{||\boldsymbol{Y}(s) - \boldsymbol{Y}_r(s)||}{||\boldsymbol{Y}(s)||} \tag{25}$$

Table II details the errors in the ROM for the associated FOM. Three different reduced orders of the ROM have been examined to determine the optimal order of the reduced system. The table illustrates that increasing the reduced order from 10 to 20 leads to an evident change in the errors. Adjusting the order to 30 shows a decline in the changes of errors. Thus, a ROM of order 20 can be considered the optimal choice for the reduced-order modelling, and this order has been preferred for the reduced system in the MOR study.

V. Conclusion

In the present work, a new reduced-order modelling method has been proposed investigating a directly coupled thermal-mechanical PEM model for its time-independent and time-dependent material nonlinearities in wires and solders. In addition to these nonlinearities, the wire and solder materials include temperature-dependent material properties, especially the coefficient of thermal expansion and Young's modulus. In this study, the second-order Arnoldi MOR approach, the Newmark time integration technique and the Newton-Raphson method for nonlinear iteration have been coupled to formulate the presented reduced-order modelling procedure. The MOR method has been used to address challenges in computing time, which occurs during the full-order modelling. The ROM demonstrates an 83% reduction in computational time requirements, with less than 1% error in DOF results. The MOR method can drastically minimise the computational time

TABLE II: Error for Reduced-Order vs. Full-Order Modelling.

Order of the ROM	**Error, $\boldsymbol{\epsilon}(s)$**
10	6.8298×10^{-13}
20	3.9239×10^{-13}
30	2.5610×10^{-13}

demands of reliability analysis while achieving the required nonlinear data for large FEM models. Future investigations will concentrate on the parametric studies of power electronic modules with material nonlinearities using the parametric model order reduction method, which explores the MOR techniques for design point explorations, owing to the necessity of several local model solutions in parametric analysis.

ACKNOWLEDGEMENT

The work is partly supported by the Engineering and Physical Sciences Research Council (EPSRC), UK, through project grant EP/R004390/1 and the multi-institutional grants EP/W006642/1, EP/W006405/1, EP/W006308/1.

REFERENCES

[1] G. Dhatt, E. Lefrançois, and G. Touzot, *Finite Element Method*. John Wiley & Sons, 2012.

[2] E. Davison, "A Method for Simplifying Linear Dynamic Systems," *IEEE Transactions on Automatic Control*, vol. 11, no. 1, pp. 93–101, 1966.

[3] R. W. Freund, "Model Reduction Methods Based on Krylov Subspaces," *Acta Numerica*, vol. 12, pp. 267–319, 2003.

[4] M. D. Eblen, "Applied FEM Techniques in Ceramic Feedthru Package Design," in *2004 Proceedings. 54th Electronic Components and Technology Conference (IEEE Cat. No. 04CH37546)*, vol. 2. IEEE, 2004, pp. 1602–1607.

[5] L. Codecasa, A. Di Costanzo, V. d'Alessandro, R. Duca, D. Gualandris, A. Morelli, F. De Viti, and C. Villa, "Towards the Extension of TRIC for Thermo-Mechanical Analysis," in *2021 27th International Workshop on Thermal Investigations of ICs and Systems (THERMINIC)*. IEEE, 2021, pp. 1–5.

[6] F. Shen and L.-L. Ke, "Numerical Study of Coupled Electrical-Thermal-Mechanical-Wear Behavior in Electrical Contacts," *Metals*, vol. 11, no. 6, p. 955, 2021.

[7] S. Feng, Y. Guo, G. Królczyk, X. Han, A. Incecik, and Z. Li, "An Engineered Solution to Multi-Physics of Insulated Gate Bipolar Transistor Module Considering Electrical-Thermal-Mechanical Coupling Effect," *Advances in Engineering Software*, vol. 175, p. 103365, 2023.

[8] J. Choi, M. Cho, and J. Rhim, "Efficient Prediction of the Quality Factors of Micromechanical Resonators," *Journal of Sound and Vibration*, vol. 329, no. 1, pp. 84–95, 2010.

[9] P. Rajaguru, M. Bella, and C. Bailey, "Applying Model Order Reduction to the Reliability Prediction of Power Electronic Module Wirebond Structure," in *2021 27th International Workshop on Thermal Investigations of ICs and Systems (THERMINIC)*. IEEE, 2021, pp. 1–6.

[10] D. Binion and X. Chen, "Coupled Electrothermal-Mechanical Analysis for MEMS via Model Order Reduction," *Finite Elements in Analysis and Design*, vol. 46, no. 12, pp. 1068–1076, 2010.

[11] C. Scognamillo, A. P. Catalano, M. Riccio, V. d'Alessandro, L. Codecasa, A. Borghese, R. N. Tripathi, A. Castellazzi, G. Breglio, and A. Irace, "Compact Modeling of a 3.3 kV SiC MOSFET Power Module for Detailed Circuit-Level Electrothermal Simulations Including Parasitics," *Energies*, vol. 14, no. 15, p. 4683, 2021.

[12] A. Schütz, S. Maeter, and T. Bechtold, "System-Level Modelling and Simulation of a Multiphysical Kick and Catch Actuator System," *Actuators*, vol. 10, no. 11, p. 279, 2021.

[13] S. Hassan, P. Rajaguru, S. Stoyanov, and C. Bailey, "Parametrising Temperature Dependent Properties in Thermal-Mechanical Analysis of Power Electronics Modules Using Parametric Model Order Reduction," in *2023 46th International Spring Seminar on Electronics Technology (ISSE)*. IEEE, 2023, pp. 1–7.

[14] S. Hassan, P. Rajaguru, S. Stoyanov, C. Bailey, and T. Tilford, "Coupled Thermal-Mechanical Analysis of Power Electronic Modules with Finite Element Method and Parametric Model Order Reduction," *Power Electronic Devices and Components*, vol. 8, p. 100063, 2024.

[15] S. Hassan, P. Rajaguru, S. Stoyanov, and C. Bailey, "Thermal-Mechanical Analysis of a Power Module with Parametric Model Order Reduction," in *2023 24th European Microelectronics & Packaging Conference (EMPC)*. IEEE, 2023, pp. 1–6.

[16] W. Witteveen and F. Pichler, "Efficient Model Order Reduction for the Dynamics of Nonlinear Multilayer Sheet Structures with Trial Vector Derivatives," *Shock and Vibration*, vol. 2014, pp. 1–16, 2014.

[17] ANSYS, "Mechanical APDL 2023 R1 - Theory Reference," 2023.

[18] J. F. Nye, *Physical Properties of Crystals: Their Representation by Tensors and Matrices*. Oxford University Press, 1985.

[19] Z. Bai and Y. Su, "Dimension Reduction of Large-Scale Second-Order Dynamical Systems via a Second-Order Arnoldi Method," *SIAM Journal on Scientific Computing*, vol. 26, no. 5, pp. 1692–1709, 2005.

[20] H. B. de Salles, L. F. F. Miguel, M. S. Lenzi, and R. H. Lopez, "Reduced-Order Model for RBDO of Multiple TMDs on Eccentric L-Shaped Buildings Subjected to Seismic Excitations," *Mechanical Systems and Signal Processing*, vol. 206, p. 110906, 2024.

[21] L. Andersson, P. Persson, and K. Persson, "Efficient Nonlinear Reduced Order Modeling for Dynamic Analysis of Flat Structures," *Mechanical Systems and Signal Processing*, vol. 191, p. 110143, 2023.

[22] A. K. Chopra, *Dynamics of Structures*, 5th ed. Harlow, England: Pearson Education Limited, 2019.

[23] M. Ashby, *Material Property Data for Engineering Materials*, 5th ed. ANSYS, Inc., 2021.

[24] T. Wierzbicki, *Structural Mechanics (Wierzbicki)*. Massachusetts Institute of Technology via MIT OpenCourseWare, 2023, https://eng.libretexts.org (Accessed 2023-July).

[25] J. Heilmann, "Lebensdauermodellierung für Gesinterte Silberschichten in der Leistungselektronischen Aufbau-und Verbindungstechnik durch Isotherme Biegeversuche als Beschleunigte Ermüdungstests," Ph.D. dissertation, Technische Universität Chemnitz, Chemnitz, Germany, 2019.

[26] M. A. Gharaibeh and J. Wilde, "Applying Anand versus Garofalo Creep Constitutive Models for Simulating Sintered Silver Die Attachments in Power Electronics," *The Journal of Strain Analysis for Engineering Design*, vol. 59, no. 1, pp. 31–43, 2024.

[27] K. C. Nwanoro, H. Lu, C. Yin, and C. Bailey, "Advantages of the Extended Finite Element Method for the Analysis of Crack Propagation in Power Modules," *Power Electronic Devices and Components*, vol. 4, p. 100027, 2023.

[28] Z. Huda, *Mechanical Behavior of Materials*. Springer, 2022.

[29] S. S. Manson, *Behavior of Materials Under Conditions of Thermal Stress*. National Advisory Committee for Aeronautics, 1953, vol. 2933.

[30] L. F. Coffin Jr, "A Study of the Effects of Cyclic Thermal Stresses on a Ductile Metal," *Transactions of the American Society of Mechanical engineers*, vol. 76, no. 6, pp. 931–949, 1954.

[31] T. Happonen, T. Ritvonen, P. Korhonen, J. Häkkinen, and T. Fabritius, "Modeling the Lifetime of Printed Silver Conductors in Cyclic Bending with the Coffin–Manson Relation," *IEEE Transactions on Device and Materials Reliability*, vol. 16, no. 1, pp. 25–29, 2015.

[32] H. Lu, C. Bailey, and C. Yin, "Design for Reliability of Power Electronics Modules," *Microelectronics Reliability*, vol. 49, no. 9-11, pp. 1250–1255, 2009.

[33] O. E. Gabriel and D. R. Huitink, "Failure Mechanisms Driven Reliability Models for Power Electronics: A Review," *Journal of Electronic Packaging*, vol. 145, no. 2, p. 020801, 2023.

[34] Q. Tao, L. Benabou, V. N. Le, N. A. T. Nguyen, and H. Nguyen-Xuan, "Temperature-Dependent Fatigue Modelling of a Novel Ni, Bi and Sb Containing Sn-3.8 Ag-0.7 Cu Lead-Free Solder Alloy," *Fatigue & Fracture of Engineering Materials & Structures*, vol. 43, no. 12, pp. 2883–2891, 2020.

[35] K. C. Nwanoro, H. Lu, C. Yin, and C. Bailey, "An Analysis of the Reliability and Design Optimization of Aluminium Ribbon Bonds in Power Electronics Modules using Computer Simulation Method," *Microelectronics Reliability*, vol. 87, pp. 1–14, 2018.

[36] R. Al Athamneh, "Reliability Modeling of Microelectronic Interconnections in Long-Term Applications," Ph.D. dissertation, Auburn University, 2019.

[37] B. Xu, Q. Lu, C. Liu, Y. Peng, K. Miao, H. Wu, R. Li, X. Li, and G. Fan, "Anisotropic Behavior and Temperature-Dependent Mechanical Properties of AA1060 Aluminum Alloy: A Comprehensive Microstructural Study," *Materials Science and Engineering: A*, p. 146550, 2024.

[38] J. Fehr and P. Eberhard, "Error-Controlled Model Reduction in Flexible Multibody Dynamics," *Journal of Computational and Nonlinear Dynamics*, vol. 5, no. 3, 2010.

[39] Q. Aumann and G. Müller, "Robust Error Assessment for Reduced Order Vibro-Acoustic Problems," *Journal of Sound and Vibration*, vol. 545, p. 117427, 2023.